Science Advances
AAAS

advances.sciencemag.org/cgi/content/full/6/29/eabb4142/DC1

Supplementary Materials for

Molding free-space light with guided wave–driven metasurfaces

Xuexue Guo, Yimin Ding, Xi Chen, Yao Duan, Xingjie Ni*

*Corresponding author. Email: xingjie@psu.edu

Published 17 July 2020, *Sci. Adv.* **6**, eabb4142 (2020)
DOI: 10.1126/sciadv.abb4142

This PDF file includes:

Supplementary Materials

1. Device fabrication

The samples were fabricated on a commercially available silicon-on-insulator wafer with 220-nm-thick (for beam steering experiments) and 500-nm-thick (for light focusing experiments) Si device layer and 3-μm buried silicon dioxide. The wafer was cleaned by sonication in acetone and IPA for 3 minutes, respectively. Alignment marker was defined by electron beam lithography with 100 kV beam (Vistec EBPG5200) followed by evaporation of 50 nm Au with a 5-nm-thick Ti adhesion layer (Kurt J. Lesker Lab-18) and lift-off. Then negative resist Fox-16 (Dow Corning Corp.) was spin-coated and prebaked at 100 °C for 4 minutes. The waveguide pattern was written followed by development in CD-26 developer (MicroChem) for 25 minutes to reduce proximity effect. Chlorine-based inductively coupled reactive ion etching (ICP-RIE) was used to etch crystalline Si with FOX-16 resist as mask (Plasma-Therm Versalock 700). The sample was immersed in buffered oxide etchant for 20 seconds followed by water rinse to remove the remaining

mask. ZEP 520A (Zeon) was spin-coated on the sample and soft-baked at 180 °C for 3 minutes. A second-step electron beam lithography was conducted to define the metasurface layer on top of the waveguide with precise alignment. The exposed sample was developed in N-amyl-acetate for 3 minutes followed by MIBK:IPA immersion for 1 minute. Au/SiO2/Au films were subsequently deposited using an electron beam evaporation system (Semicore). The pattern was then lifted off in 1165 remover (MicroChem) at 85 °C in water bath for 2 hours. The sample was finally diced along the input port of waveguide for measurement.

The OAM micro-ring laser was fabricated on InGaAsP (500 nm, multi-quantum-well layer) / InP substrate. First the micro-ring resonator was defined by electron beam lithography with FOX-16 negative resist. The resist acted as an etch mask in the BCl_3 based ICP-RIE process. Then the sample was immersed in buffered oxide etchant to remove the mask. A second-step electron beam lithography using ZEP 520A resist was performed with precise alignment to define the metasurface layer on top of the micro-ring resonator. A sequential electron beam evaporation was done to deposit Au/Si/Au films, followed by a standard lift-off process in 1165 remover at 85 °C in water bath for 2 hours.

2. Simulation methods

2.1 Metal / dielectric / metal nano-bar antenna design

Numerical simulations were carried out using a commercially available finite element method (FEM) solver package – COMSOL Multiphysics. Third-order finite elements and at least 10 mesh steps per wavelength were used to ensure the accuracy of the calculated results. We simulated individual Metal / dielectric / metal meta-atoms first. We used an eigenmode solver to find the TE_{00} mode of the silicon waveguide as well as its modal

index at 1550 nm wavelength. Then this modal index was used in the model to further calculate the phase and amplitude of the extracted light by monitoring the field at a few wavelengths over the waveguide. The antenna is centered on top of the waveguide. We swept the geometrical parameters of the meta-atoms and monitored the phase and amplitude of the scattered wave into free space and obtained the phase and amplitude maps/contours as shown in Fig. 2B and Fig. S7A. The trapezoidal shape of meta-atoms resulted from our nanofabrication was also considered in our model to get accurate design parameters.

2.2 Device level full-wave simulations

In order to simulate the beam steering, a full device model that consists of an array of meta-atoms placed on top of Si waveguide was established. The meta-atoms were distributed along the waveguide so that they formed a linear phase gradient (Fig. 2D). In a similar fashion, an array of meta-atoms fulfilling the spatial phase distribution of a lens were placed on top of Si waveguide to simulate the light focusing effect (Fig. 4A).

A device-level model of metasurface incorporated micro-ring resonator was constructed to simulate the OAM radiation. Four Au/Si/Au meta-atoms selected from calculated phase and amplitude maps/contours (Fig. S7A) were used to construct a supercell. 58 supercells ($N = 58$) were placed on top of the resonator. Using the WGM with $M = 59$, we achieved OAM radiation with topological charge of +1 according to Eq. (4). Fig. S7B illustrates the electric field distribution of TE_{00} mode which shows the typical standing wave pattern formed by the two counter-propagating (CW and CCW) WGMs. The extracted light in free space carries OAM as shown in Fig. 5B.

3. Study of the resonant properties of metal / dielectric / metal nano-bar antenna

Two different antennas designs were used in this work: (i) Au/SiO_2/Au sandwiched nano-bar antennas on Si waveguide (Fig. 2B); and (ii) Au/Si/Au sandwiched nano-bar antennas on InGaAsP waveguide (Fig. S7A). To explore the origin of large phase shift range (over 2π) of the sandwiched nanoantenna design, we performed parametric sweep of the wavelength on Au/SiO_2/Au antenna (l_x = 150 nm, l_y = 280 nm). The scattering phase induced by the nanoantenna was calculated by subtracting the phase obtained from simulations with nanoantenna to that without nanoantenna. As shown in Fig. S1B, the phase shift of nanoantenna changes by 2.6π from 1440 nm to 1550 nm. In addition, we simulated the eigenmodes of the Au/SiO_2/Au antenna (l_x = 150 nm, l_y = 280 nm) in air, and observed an electric dipole resonance (ED) at 1400nm and a magnetic dipole (MD) resonance at 1800nm (Fig. S1A, middle panel). Placing the nanoantenna on the waveguide, we then simulated its field distribution at 1510 nm (Fig. S1A, right panel) where a large phase shift happened in Fig. S1B. Clearly, the TE_{00} waveguide mode excites the eigenmodes (ED and MD) of the nanoantenna. The electric field and magnetic field distributions show characteristics of the ED and MD resonances, validating that the overlap of two resonances create the phase shift range over 2π.

4. Study of the efficiency and loss of guided-wave-driven metasurface

To evaluate the up-extraction and focusing efficiency, we conducted full-wave simulations using COMSOL Multiphysics and Lumerical FDTD (finite-difference time-domain). Extraction efficiency was calculated by dividing the surface integrated power flow from a surface above the waveguide to the input power. And ohmic loss was estimated by dividing the volume integration of the power dissipation in nanoantennas to the input

power (Fig. S2). For beam deflection, the power loss due to back reflection R is small and most of the loss is induced by the metallic antenna absorption. From the simulation, we extracted the up-extraction efficiency per supercell $\eta_e \sim 0.1\%$ and the total dissipation per supercell $\eta_t \sim 1.1\ \%$. According to the following equation:

$$efficiency = (1 - R)\frac{\eta_e}{\eta_t}(1 - e^{-\eta_t l}) \quad \text{(S.1)}$$

where l is the number of supercells. As a rough estimation, the maximum up-extraction efficiency can be approximated as $\eta_e / \eta_t \sim 9\ \%$ (Fig. S2B). To calculate the focusing efficiency, the model consisting of 17.4 μm long silicon waveguide and 65 nanoantennas was simulated (Fig. S2C). The focusing efficiency is about 10%, and the absorption loss is 45.5%.

In order to reduce the metal induced loss, we designed pure dielectric $SiO_2/Si/SiO_2$ (thickness: 100/400/100 nm) antennas that not only fulfil over π phase control but also exhibit no material loss in the telecommunication wavelengths range (Fig. S3). Three $SiO_2/Si/SiO_2$ sandwiched antennas were selected to construct one supercell to achieve beam deflection function. We simulated the full device and extracted its parameters. The up-extraction efficiency per supercell η_e is around 0.0945% which is similar to that of the $Au/SiO_2/Au$ nanoantennas array. But the total dissipation per supercell η_t of 0.117% is ten times less due to the absent of metallic components. The maximum up-extraction efficiency can be approximated as $\eta_e / \eta_t \sim 80\ \%$ (Fig. S3C).

It should be noted that the design is based on a perturbation condition where the nanoantenna does not disrupt the guided mode. This is confirmed by the simulations above where the out-coupling efficiency induced by one supercell is on the order of 0.1% for both Au/SiO2/Au antenna and Si/SiO2/Si antenna design. To significantly disrupt the guided waves, such as realizing mode conversion, the array of nanoantennas must exhibit

specific phase gradient to compensate the momentum difference between the original guided mode and the ultimate converted one. However, our nanoantennas do not fulfill this function, which makes it rather difficult or impossible to convert the fundamental mode to other modes. In addition, our nanoantennas are symmetric and placed in the center of the waveguide, so they don't have good overlap with high order waveguide modes, thus impeding effective mode conversion. This is also confirmed by the FDTD simulation on the mode purity analysis after the TE_{00} mode interact with 150 nanoantennas (50 supercells). The conversion efficiencies to TM_{00} and TE_{10} are 6.5×10^{-7} % and 1.5×10^{-5} %, respectively, which might be due to numerical error. The conversion efficiency to TM_{10} and TE_{20} is on the order of 0.1%, which is negligible. Therefore, we can safely assume that the dominant mode that interacts with the nanoantennas is TE_{00} mode.

5. Characterization of beam steering and focusing on waveguide-fed metasurfaces

We characterized our waveguide-fed metasurfaces with beam steering and focusing functions using the optical setup shown in Fig. S4. A free-space laser beam output from a Ti:Sapphire laser pumped optical parametric oscillator (OPO) was coupled into a commercially available tapered lensed single-mode fiber. The focused laser beam from the tapered fiber was coupled into the input port of our fabricated ridge waveguide sample in end-fire manner by using a three dimensional (3D) translational stage. The coupled-in light propagated through a triangle taper linking the input port and the single-mode waveguide, during which the high-order modes vanished, and only fundamental transverse electrical mode survived. The light scattered into free space by metasurfaces on top of the single-mode waveguide was collected by an objective (N.A. = 0.95) and then transmitted

through a tube lens. Part of the light was reflected by a beamsplitter for real-space imaging. And the light transmitted through the beamsplitter was focused by a Bertrand lens to form *Fourier-space* image. In off-chip beam-steering measurement, the laser wavelength was tuned using the OPO to acquire wavelength-dependent beam steering angles. In addition, Fourier-space images were taken by coupling 1550nm laser beam into samples with different supercell periods. After that, the scattering angles were extracted from the Fourier-space images calibrated by a ruled reflective grating (grooves density of 600/mm). In off-chip focusing measurement, the samples were mounted on a 3D translational stage with a high-resolution piezo-controlled actuator in *z*-direction. By moving the *z* stage, the real-space images were taken at different distance from the waveguide plane and a 3D intensity distribution was reconstructed.

As shown in Fig. S5, the focal point shifts towards the input port as the wavelength increases. According to equation (2) in the main text, the required phase shift for nanoantenna at position x is $\Delta\Phi(x) = -k_0\sqrt{x^2 + f^2} - \beta x$ (the designed wavelength is 1.55 μm). As wavelengths increase, both k_0 ($2\pi/\lambda$) and β will decrease, so that the designed phase shift is smaller than the required phase shift at longer wavelength. The opposite argument is true when the wavelength decreases. Taking the three wavelengths 1.5 μm, 1.55 μm and 1.6 μm as an example (simulations in Fig. S5), in order to compensate the difference between the phase distribution at designed wavelength (1.55 μm) and that of the operating wavelength, the focal position has to shift accordingly, so that $\Delta\Phi_{1.6}(x) \approx \Delta\Phi_{1.55}(x) \approx \Delta\Phi_{1.4}(x)$.

$$\Delta\Phi_{1.5}(x) = -k_{1.5}\sqrt{(x - dx_1)^2 + f^2} - \beta_{1.5}x$$

$$\Delta\Phi_{1.55}(x) = -k_{1.55}\sqrt{x^2 + f^2} - \beta_{1.55}x$$

$$\Delta\Phi_{1.6}(x) = -k_{1.6}\sqrt{(x + dx_2)^2 + f^2} - \beta_{1.6}x$$

Therefore, the focal point position of longer wavelength shifts towards the input port.

6. Characterization of OAM lasing on waveguide-fed metasurfaces integrated InGaAsP/InP micro-ring resonator

Fig. S8 shows the experimental setup to observe the lasing spectra and to confirm the OAM properties of the laser radiation. In our experiment, a femtosecond pulsed laser (~140 fs, repetition rate 80 MHz) at 900 nm wavelength was reflected by a dichroic mirror and then focused by a Newport 20X objective (NA = 0.40) onto the micro-ring resonator. The pump power was controlled by a circular variable neutral density filter and monitored by a power meter. The lasing emission was collected by the same objective and then transmitted through the dichroic mirror and detected by a spectrometer (Horiba), a far-field imaging system and a Michelson interferometry setup. With a flip mirror to switch the paths, the laser emission was either sent into the spectrometer/imaging system or the interferometry setup. In the interferometry setup, the laser emission was split into two beams by a pellicle beam splitter, and then recombined with an off-center beam overlap to form an interference pattern recorded by an infrared camera. A delay line was used in order to balance the optical path lengths of the two arms.

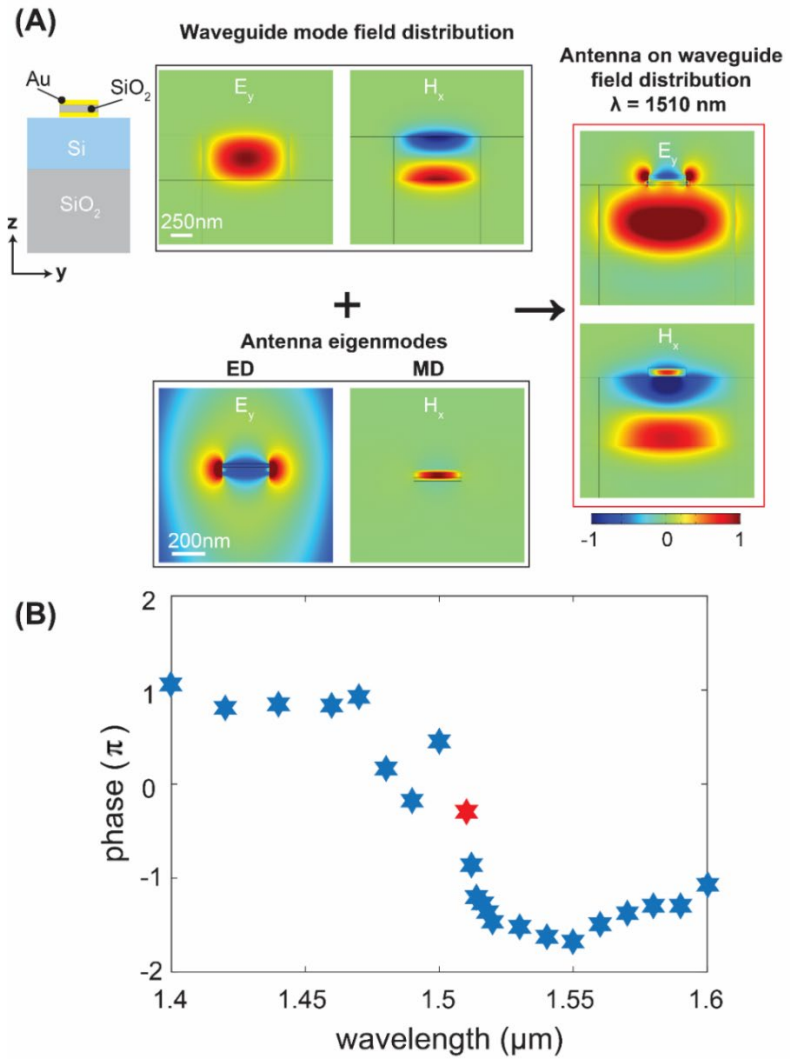

Fig. S1. Resonance analysis of metal/dielectric/metal nanoantennas excited by guide waves. (**A**) Simulated field distribution of silicon waveguide, Au/SiO_2/Au sandwiched nanoantennas (l_x = 150nm, l_y = 280nm) and the integrated systems. The antenna exhibits electric dipole (ED) and magnetic dipole (MD) eigenmodes at 1400nm and 1820nm, respectively. At 1510 nm, the integrated system exhibits electric field and magnetic field distributions characteristic of the ED and MD, validating that the overlap of two resonances create the phase shift range over 2π. (**B**) Calculated scattering phase induced by Au/SiO_2/Au sandwiched nanoantennas (l_x = 150nm, l_y = 280nm) at different wavelengths, showing a phase shift range greater than 2π.

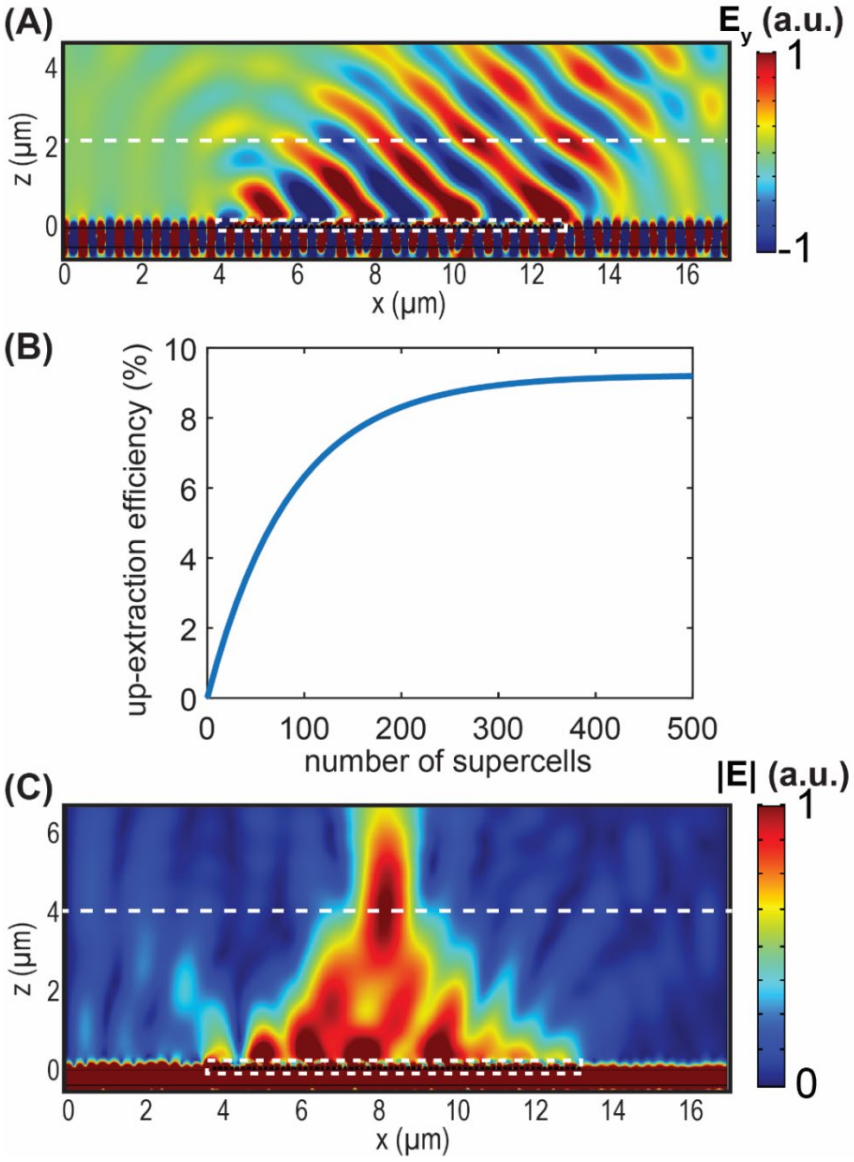

Fig. S2. Efficiency study of guided-wave-driven metasurfaces consisting of Au/SiO_2/Au meta-atoms. (**A**) Simulated electric field (E_y) distribution of the guided-wave-driven metasurface (20 sets of supercells, 60 nanoantennas) for beam deflection. (**B**) Calculated up-extraction efficiency based on equation S1. The up-extraction plateaued around 9%. (**C**) Simulated normalized electric field (|E|) distribution of the guided-wave-driven metasurface (65 nanoantennas) for focusing. In both figures, the dashed line indicates the surface that the Poynting vector was integrated, and the dashed white rectangle marks the metasurface region.

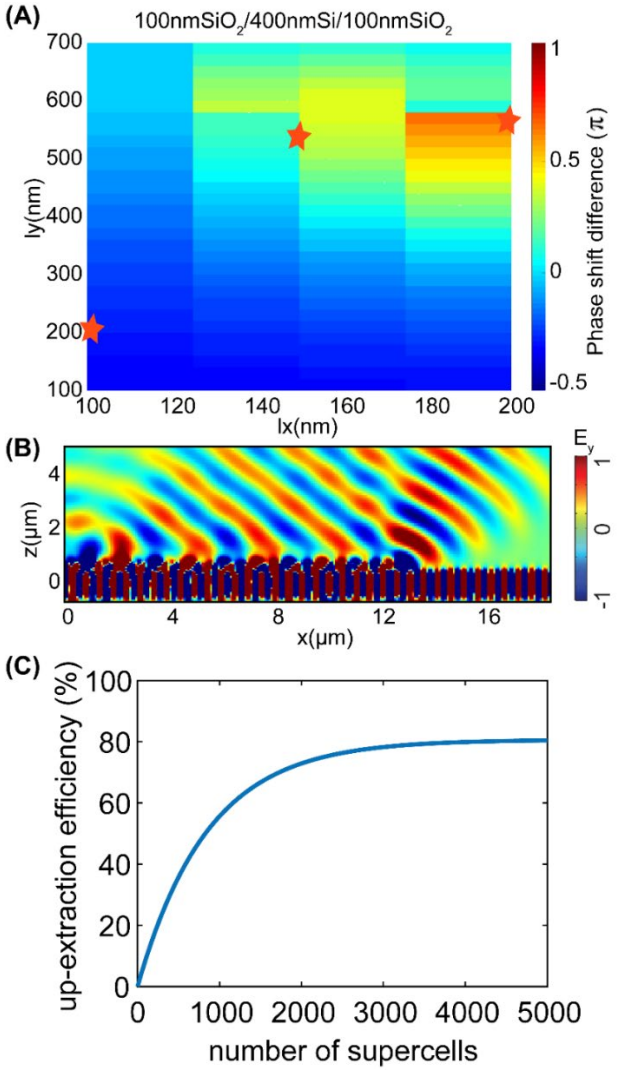

Fig. S3. **Efficiency study of guided-wave-driven metasurfaces consisting of SiO_2/Si/SiO_2 meta-atoms.** (**A**) A pseudo-color map of the simulated phase shifts generated by SiO_2/Si/SiO_2 nanoantennas with different lengths (l_x) and widths (l_y). Three meta-atom designs (marked by the red stars) with a constant phase shift difference of 2π/3 were selected to construct the supercell used in simulation of beam deflector shown in (**B**). (**B**) Simulated electric field (E_y) distribution of the guided-wave-driven metasurface beam deflector using designs of (**A**) (20 sets of supercells, Λ = 680nm). (**C**) Calculated up-extraction efficiency based on equation S1. The up extraction plateaued around 80%.

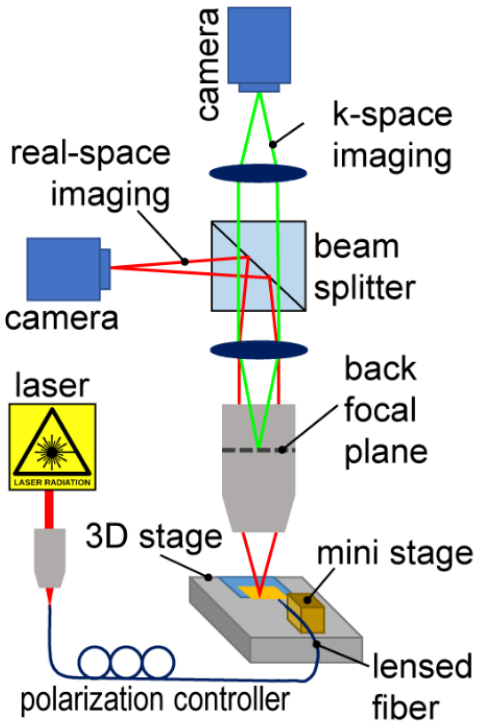

Fig. S4. **Experimental setup for the off-chip beam steering and focusing measurements.** A free-space laser beam emitted from a Ti:Sapphire laser pumped OPO was coupled into a tapered lensed single-mode fiber and then to the input port of the sample. The extracted light in free space was collected by an objective (NA = 0.95) and then transmitted through a tube lens. The light was partially reflected by a non-polarizing beam splitter for real-space imaging. And the rest light was transmitted through the beam splitter and was focused by a Bertrand lens to form *Fourier-space* images.

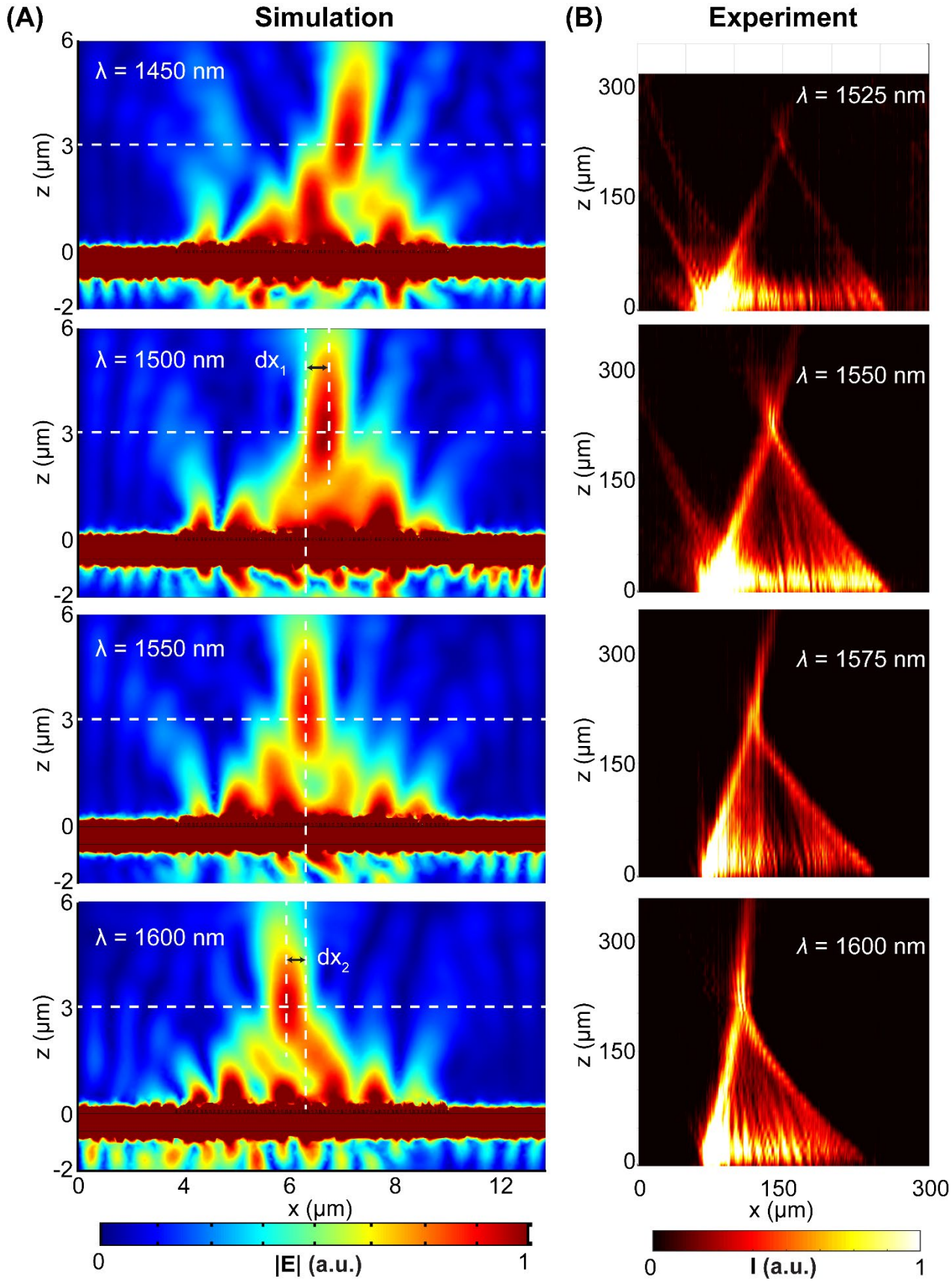
(A)
Simulation
(B)
Experiment
λ = 1450 nm
λ = 1500 nm
dx1
λ = 1550 nm
λ = 1600 nm
dx2
z (μm)
x (μm)
|E| (a.u.)
λ = 1525 nm
λ = 1550 nm
λ = 1575 nm
λ = 1600 nm
I (a.u.)

Fig. S5. Focusing performance of guided-wave-driven metasurfaces at different wavelengths. (**A**) Simulated and (**B**) experimentally measured guided-wave-driven off-chip focusing at different wavelengths. The focal distance of simulated device is 3 μm, and the focal distance of the sample is 225 μm.

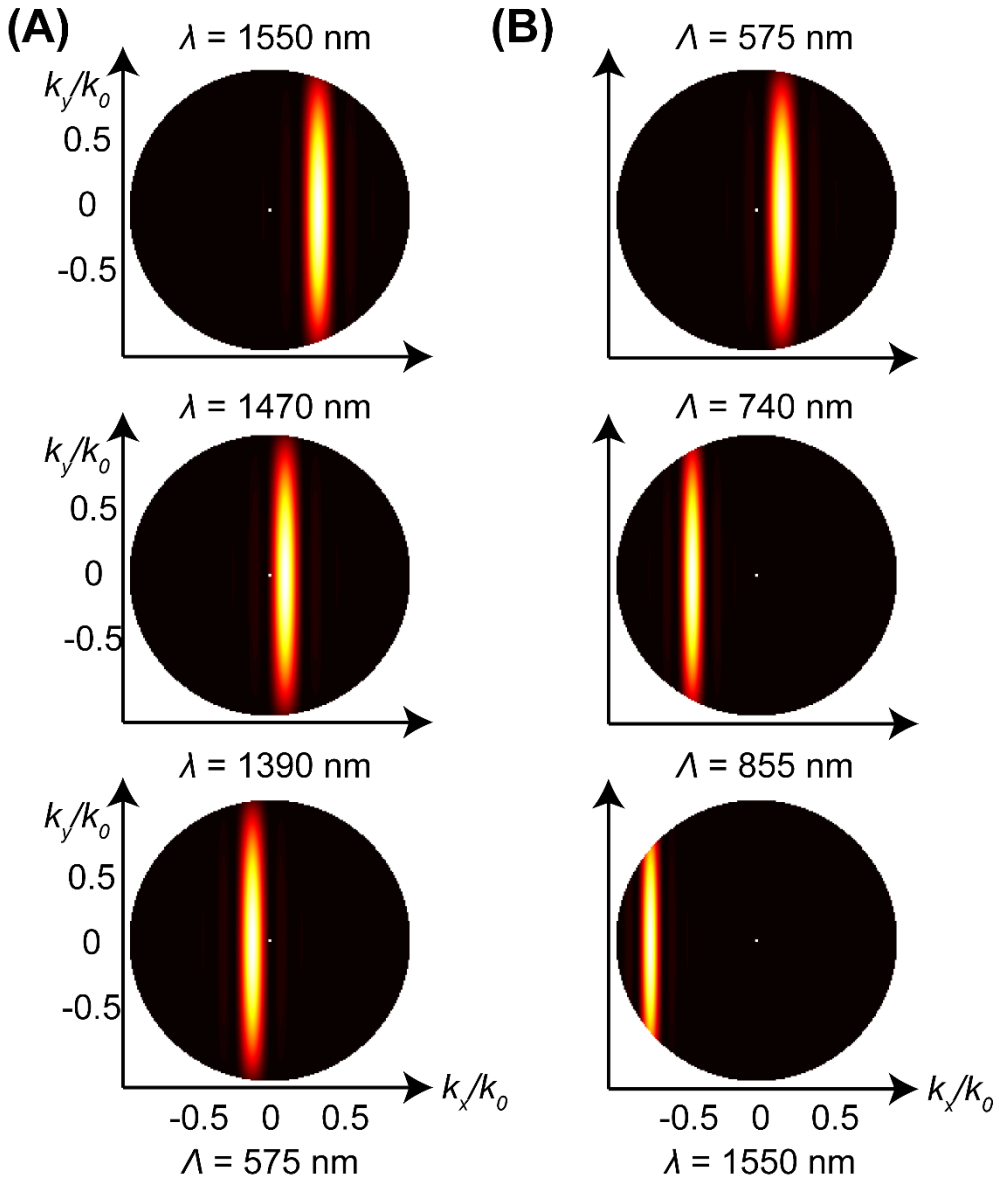

Fig. S6. Fourier-space analysis of off-chip beam steering. (**A**) Simulated Fourier-space images of the extracted light at different wavelengths from a metasurface with supercell size of 575 nm. (**B**) Simulated Fourier-space images of the extracted light from metasurfaces with different supercell sizes at 1550 nm wavelength.

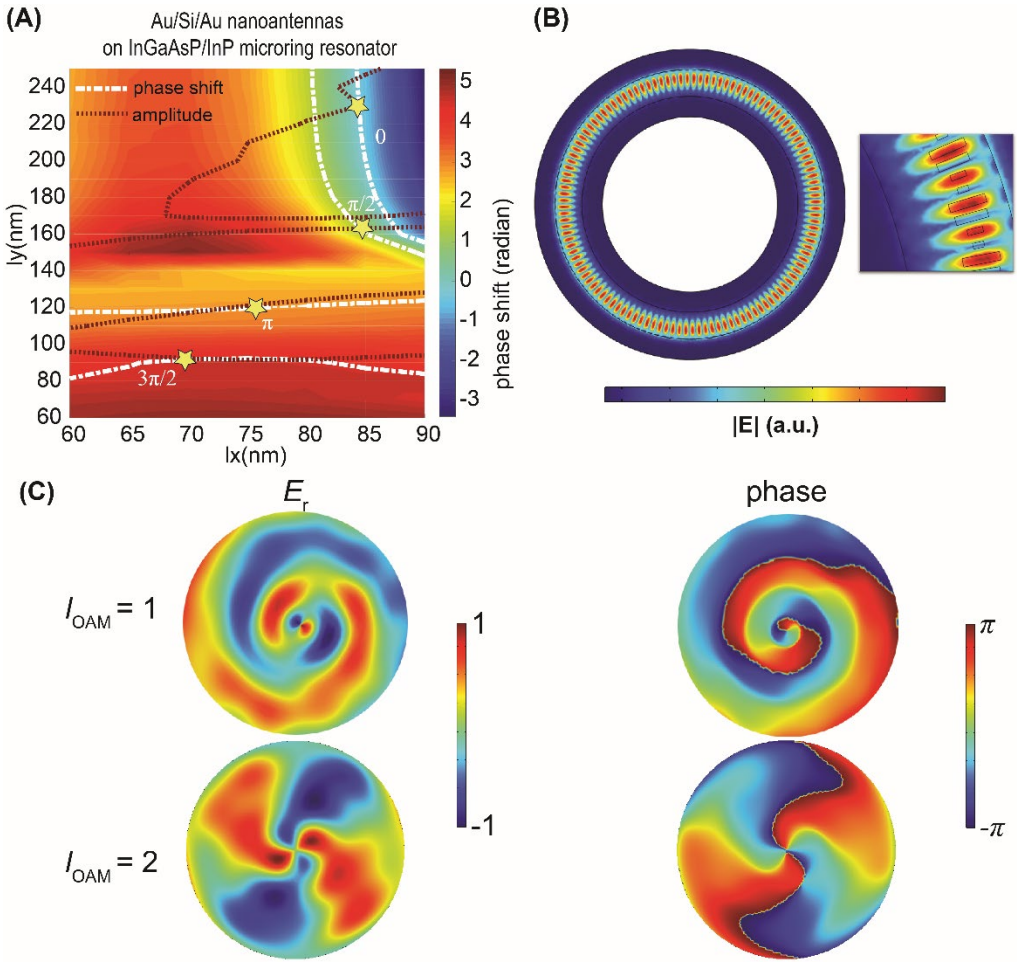

Fig. S7. Design of meta-atoms for orbital angular momentum microring laser. (**A**) A pseudo-color map of the simulated abrupt phase shifts overlaid with amplitude contours generated by the Au/Si/Au meta-atoms with different lengths (l_x) and widths (l_y). Four meta-atom designs (marked by the yellow stars) with a constant phase shift difference of π/2 were selected to construct the metasurface supercell. The black dashed line is the contour of the extracted electric field amplitude of 2×10^5 V/m. (**B**) The simulated electric field distribution of the micro-ring resonator (diameter = 9 μm, width = 1.1 μm and height = 1.5 μm) with WGM order M = 59. A close-up view of one segment of the micro-ring shows a good spatial overlap between the waveguide mode and the meta-atoms. (**C**) Simulated electric field (radial component) and phase distribution of emitted wave with

different numbers of metasurface supercells N. The azimuthal order of the WGM is M = 59 at the resonant wavelength of 1550 nm, and the number of supercells is N = 58 (top row) and N = 57 (bottom row). The resulting topological charge of the OAM radiation can be seen by the number of 2π phase evolution along the circumference, which is +1 (top row) and +2 (bottom row), respectively.

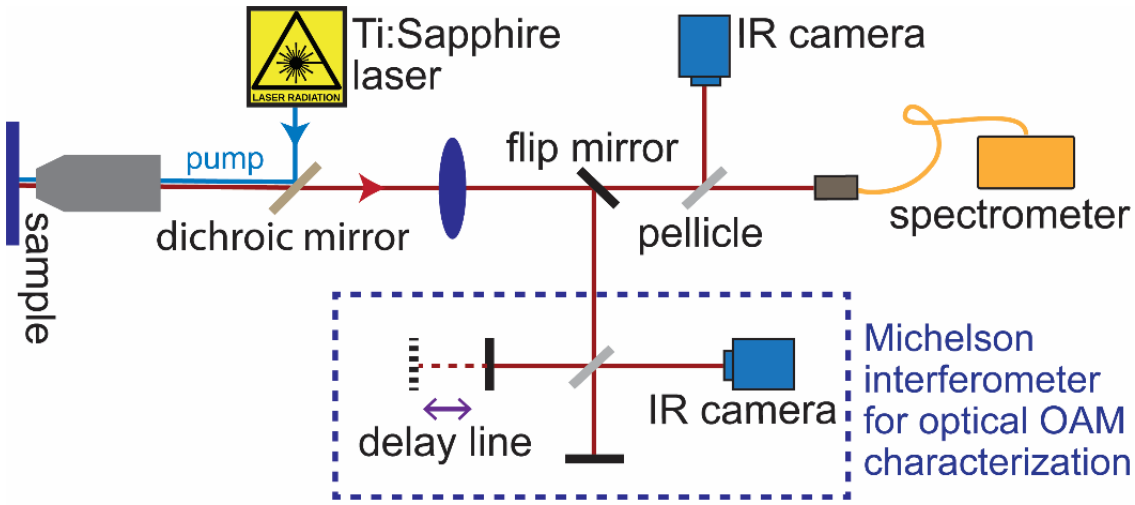

Fig. S8. Experimental setup for characterizing the OAM laser emission. A femtosecond pulsed pump laser (~140 fs, repetition rate 80 MHz) at 900 nm wavelength was reflected by a dichroic mirror and then focused by a Newport 20X objective (NA = 0.40) onto the micro-ring resonator. The lasing emission was collected by the same objective and then transmitted through the dichroic mirror to be detected by a spectrometer, a far-field imaging system and a Michelson interferometry setup. A flip mirror was used to switch the paths.